ORIGINAL PAPER

Bi$_2$S$_3$ for sunlight-based Cr(VI) photoreduction: investigating the effect of sulfur precursor on its structural and photocatalytic properties

Nicolas Perciani de Moraes[1] · Pedro Malavota Ribeiro[2] · Bruno Henrique Baena da Silva[2] ·
Tiago Moreira Bastos Campos[3] · Gilmar Patrocínio Thim[3] · Marcos Roberto de Vasconcelos Lanza[1] ·
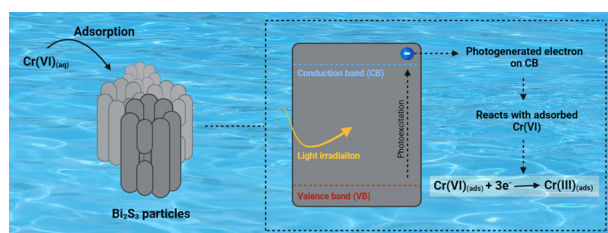Liana Alvares Rodrigues[2]

Abstract

This study investigated the suitability of multiple bismuth sulfide (Bi$_2$S$_3$) samples for the photoreduction of Cr(VI) under simulated sunlight, aiming to elucidate the effect of different sulfide sources (thiourea, thioacetamide, sodium sulfide, potassium sulfide, and ammonium sulfide) on the final structural and photocatalytic properties of this semiconductor. The sulfides were produced through simple precipitation methods, without the necessity of complex methodologies or equipment. Additionally, the effect of thermal treatment on the properties of the Bi$_2$S$_3$ samples was also evaluated. The choice of the sulfide precursor imparted distinct characteristics onto the synthesized Bi$_2$S$_3$, such as distinct morphologies, specific surface areas (SSA), and crystalline structures. Notably, the efficiency of Cr(VI) photoreduction was found to be intricately linked to the adsorption capacity of Bi$_2$S$_3$. In this context, the calcination process emerged as a significant impediment, as it substantially diminished both the SSA and adsorption capacity of the materials. Among the sulfide sources investigated, Bi$_2$S$_3$ synthesized using K$_2$S exhibited superior photoreduction efficiency, attributed primarily to its remarkable adsorption capacity and rod-like morphology. The photoreduction mechanism was determined to be carried out by the direct reaction between Cr(VI) and photogenerated electrons. Regarding operational parameters, initial concentration, pH and temperature had major effects on the photoreduction efficiency; high initial concentrations led to the saturation of the active sites and lower reaction rate constants, whereas lower pHs and higher temperatures favored the photoreduction process. As for the recycle tests of the best photocatalyst, it was discovered a significant efficiency loss between cycles, which was linked to the occlusion of active sites through the formation of chrome-based species on the surface of the photocatalyst.

Graphical Abstract

✉ Liana Alvares Rodrigues
liana.r@usp.br

1 São Carlos Institute of Chemistry, University of São Paulo, São Carlos, SP, Brazil

2 Lorena School of Engineering- EEL/USP, Estrada Municipal do Campinho S/N, Lorena, SP, Brazil

3 Instituto Tecnológico de Aeronáutica-ITA/CTA, São José dos Campos, São Paulo, Brazil

Highlights

- Morphology and structure were affected based on the sulfur precursor employed;
- Photoreduction of the Cr(VI) was strongly linked to the adsorption capacity;
- The calcination process was unfavorable due to the reduction of surface area.

1 Introduction

Currently, hexavalent chromium (Cr(VI)) contamination in aquatic environments has become a pressing concern worldwide [1]. The discharge of this toxic compound into water bodies originates predominantly from industrial processes such as metal plating, leather tanning, and textile manufacturing, posing significant risks to both aquatic ecosystems and human health [2, 3]. Cr(VI) is known to accumulate in aquatic organisms, leading to biomagnification up the food chain and potentially affecting entire ecosystems [4]. Moreover, its carcinogenic properties raise alarms for human populations reliant on contaminated water sources for drinking, irrigation, and recreational activities [4, 5]. Efforts to mitigate Cr(VI) contamination involve stringent regulations on industrial discharges, the development of advanced treatment technologies, and extensive monitoring programs to safeguard water quality and public health Top of Form [2, 6, 7].

Considering novel and efficient remediation techniques, heterogeneous photocatalysis stands out as a promising method for addressing the pervasive issue of Cr(VI) contamination in aqueous environments [8]. This advanced oxidation process harnesses the power of light-sensitive catalysts to facilitate the reduction of Cr(VI) to its less harmful form, Cr(III), through a series of photochemical reactions [9]. The mechanism involves the generation of electron-hole pairs upon exposure to light, which initiate redox reactions with Cr(VI) species present in the water matrix leading to their conversion into Cr(III), which is significantly less toxic and exhibits lower mobility and bioavailability in aquatic systems [10]. This process offers several advantages, such as its relatively low operational costs and its environmental compatibility, as it does not require the addition of harsh reducing agents, such as sulfur dioxide gas or sodium bisulfite [11, 12]. Furthermore, ongoing research focuses on enhancing the efficiency and scalability of photocatalytic systems, optimizing catalyst properties, and exploring novel reactor designs to facilitate their practical application for large-scale remediation projects [13].

In this context, metal sulfides have recently garnered significant attention as promising photocatalysts for various photoreduction processes, owing to their advantageous properties, such as low bandgap energy and suitable electronic structure [14]. Among these, bismuth sulfide (Bi_2S_3) emerges as a particularly intriguing candidate due to its unique characteristics [15]. Bi_2S_3 exhibits a low bandgap energy (ranging from 1.3 to 1.7 eV), enabling it to absorb a broad spectrum of light, encompassing the entire visible and near-infrared regions [16]. This exceptional light-absorbing capability facilitates the efficient utilization of natural sunlight for photocatalytic reactions, including the reduction of Cr(VI) to Cr(III) [17]. Moreover, the simplicity of synthesis of the bismuth sulfide makes it an attractive option for practical applications in environmental remediation, whereas its tunable properties, including its morphology, surface area, and electronic structure, offer opportunities for optimizing its photocatalytic performance [17, 18].

Therefore, this study aims to comprehensively assess the effectiveness of Bi_2S_3 as a photocatalyst for the photoreduction of Cr(VI) in aqueous solutions, utilizing simulated sunlight as the irradiation source. The investigation will encompass a systematic exploration of various sulfide precursors and calcination conditions to tailor the structural and morphological properties of the Bi_2S_3 photocatalysts. Through detailed characterization techniques such as X-ray diffraction (XRD), scanning electron microscopy, and UV-visible spectroscopy, the influence of sulfide precursors and calcination on the crystalline structure, surface morphology, and optical properties of Bi_2S_3 will be elucidated. Furthermore, the photocatalytic performance of the synthesized materials will be evaluated through batch experiments, focusing on parameters such as initial concentration, pH, temperature, and recycling. Insights gained from this investigation will contribute to advancing our understanding of the fundamental mechanisms underlying the photocatalytic reduction of Cr(VI) by Bi_2S_3 and pave the way for the development of highly efficient photocatalytic systems for environmental remediation applications.

2 Materials and methods

2.1 Synthesis of the bismuth sulfide (Bi_2S_3)

Initially, 9.7 g of bismuth nitrate pentahydrate ($Bi(NO_3)_3 \cdot 5H_2O$, 99% w/w, CAS N° 10035-06-0) was weighed in a beaker; then, 5 ml of nitric acid (HNO_3, 65% w/w, CAS N° 7697-37-2) was added, followed by the slow addition of 10 ml of deionized water. The above-described procedure was repeated five times to synthesize distinct materials. For the first material, 3 g of thioacetamide (CH_3CSNH_2, 99% w/w, CAS N° 62-55-5) was solubilized in 50 ml of deionized

water. This solution was then added to the previously prepared bismuth nitrate solution. Similarly, the other materials were synthesized using the following quantities of sulfide precursor: 3 g of thiourea ((NH$_2$)$_2$CS, 99% w/w, CAS N° 62-56-6), 15 g of sodium sulfide (Na$_2$S, 32–38% w/w, CAS N° 1313-82-2), 10 g of potassium sulfide (K$_2$S, 44% w/w, CAS N° 39365-88-3), and 13.6 mL of ammonium sulfide ((NH$_4$)$_2$S, 20% w/w, CAS N° 12135-76-1). The solutions obtained using thioacetamide and thiourea were kept in an oven at 100 °C for 24 h, in closed containers, in order to promote the full precipitation of the sulfides. The precipitates obtained were filtered and washed until pH = 7 was observed in the filtrate, then dried in an oven at 100 °C for 24 h. The dried samples were subsequently sieved using a 325-mesh sieve and calcined at 300 °C (30 min) in a muffle furnace, under a nitrogen gas flow (0.5 L min^{-1}).

2.2 Characterization

X-ray diffractograms were obtained using a PANalytical Empyrean diffractometer. Rietveld refinement was performed using the Profex software suit. Scanning electron micrographs were captured using the TESCAN Vega 3 XMU microscope. Diffuse reflectance spectroscopy was performed in a Shimadzu UV-2600 equipped with an integrating sphere. Specific surface area (SSA) was measured through BET analysis in a V-Sorb 2800 P (GoldApp) analyzer. Chronoamperometry was performed using a PGSTAT204 Autolab Metrohm potentiostat in a 3-electrode electrochemical system. The experiments were conducted within a single-compartment quartz electrochemical cell with a volume of 0.2 L and 0.8 V (vs Ag/AgCl), with 0.1 mol L^{-1} K$_2$SO$_4$ electrolyte. Infrared spectroscopy utilized a universal attenuated total reflectance sensor, with analysis performed using a Perkin Elmer Frontier spectrometer operating in the range of 4000 to 600 cm^{-1} at a resolution of 4 cm^{-1}. The point of zero charge was determined as described by Ribeiro et al. [19].

2.3 Photocatalytic reduction of Cr(VI)

The Cr(VI) photoreduction experiments were conducted in a cooled jacketed batch reactor (height = 10 cm, internal diameter = 10 cm, T = 25 °C), filled with 500 mL of Cr(VI) solution (C$_0$ = 10 mg L^{-1}). For each test, 0.1 g of photocatalyst was used and a uniform suspension was obtained through magnetic stirring. 2 mL samples were collected at predetermined times and filtered through 0.22 μm nylon filters. The concentration of Cr(VI) was determined using the diphenyl carbazide method, monitoring absorbance at 540 nm with a Shimadzu UV-2600 spectrophotometer [20]. To that intention, 0.5 mL of each sample was mixed with 2 mL of deionized water and 0.04 mL of sulfuric acid (10% v/v) and

diphenyl carbazide (0.65% w/w, in acetone) solutions. The system was initially kept in the dark to ensure adsorption-desorption equilibrium was achieved prior to the photocatalytic tests. Subsequently, an artificial sunlight source (Osram Ultra-Vitalux 300 W) was activated (positioned 10 cm above the reactor). The photon flux on the surface of the reactor was measured as 1950 μmol$_{photons}$ m^{-2} s^{-1} using an Apogee Original X Quantum Sensor.

3 Results and discussion

3.1 Characterization

Figure 1 shows the X-ray diffractograms for the synthesized materials.

According to the XRD data collected, the materials synthesized using K$_2$S, Na$_2$S, and (NH$_4$)$_2$S are predominantly amorphous before the calcination process, whereas the materials synthesized using thiourea and thioacetamide presented the orthorhombic bismuth sulfide structure (JCPDS N°170320) [18]. In particular, the material synthesized using K$_2$S had peaks related to the orthorhombic sulfur (JCPDS N°08-0247, marked by blue circles) prior to calcination. Following the calcination process, the XRD analysis revealed the emergence of the orthorhombic bismuth sulfide crystal structure in all of the synthesized samples. This transformation underscores the significant impact of calcination on the structural evolution of the photocatalysts, particularly in inducing the crystallization of the previously amorphous samples. Furthermore, the identification of the orthorhombic bismuth sulfide structure as the single phase present post-calcination corroborates the successful synthesis and phase purity of the photocatalysts.

In the context of photocatalysis, the atomic arrangement within crystalline materials plays a pivotal role in enhancing their efficiency. The well-defined lattice structure of crystalline materials promotes efficient charge separation upon photon absorption, as the spatial organization facilitates the migration of photogenerated electron-hole pairs to the material's surface, where redox reactions take place [21]. Conversely, amorphous materials, lacking a long-range order in their atomic arrangement, possess unique advantages that render them effective photocatalysts as well. One notable advantage is their typically higher surface area compared to their crystalline counterparts. The absence of a defined crystalline lattice allows for a more disordered structure, which in turn results in a higher density of surface defects and active sites available for adsorption and catalytic reactions. This increased surface area enhances the accessibility of reactant molecules to the catalytic sites, thereby facilitating the adsorption step of the photoreduction mechanism [22].
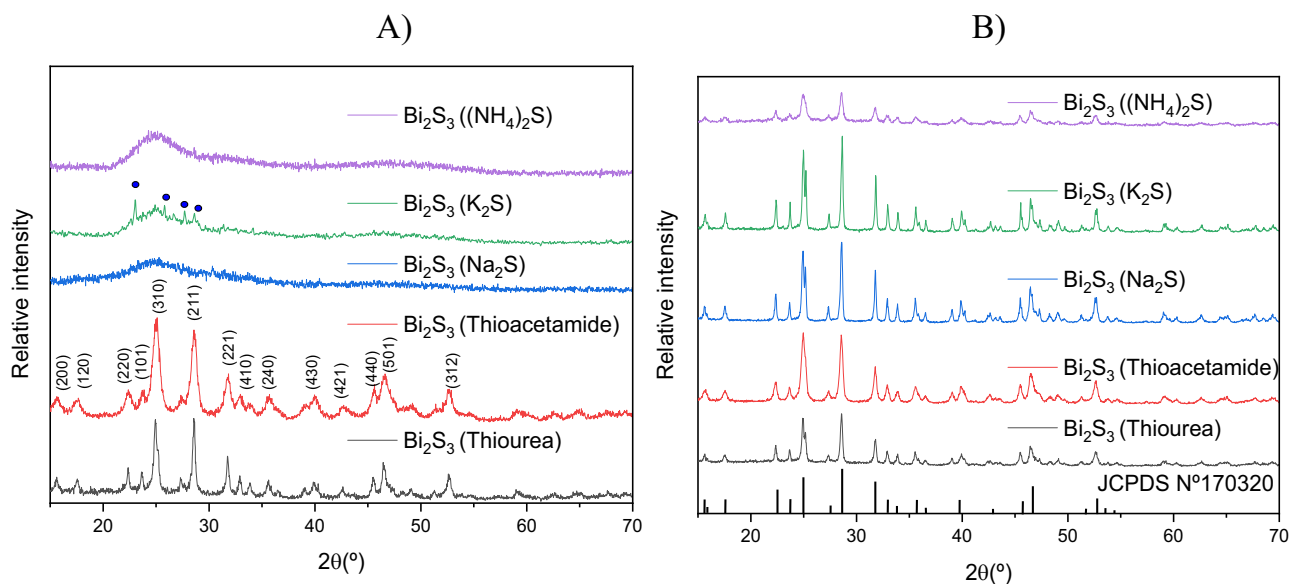
A) B)

Fig. 1 X-ray diffractograms for: **A** Uncalcined materials; **B** Calcined materials

Table 1 Rietveld refinement results obtained for the different Bi$_2$S$_3$ samples

Material	a	b	c	α	β	γ	Lc (nm)
Bi$_2$S$_3$ (Thioacetamide)	0.400	1.121	1.162	90.9	90.9	89.685	42.44
Bi$_2$S$_3$ (Thiourea)	0.398	1.118	1.162	90.9	90.9	89.795	51.20
Bi$_2$S$_3$ (K$_2$S, 300 °C)	0.398	1.117	1.162	90.9	90.9	89.783	146.1
Bi$_2$S$_3$ (Na$_2$S, 300 °C)	0.399	1.118	1.162	90.9	90.9	89.763	130
Bi$_2$S$_3$ ((NH$_4$)$_2$S, 300 °C)	0.399	1.117	1.162	90.9	90.9	89.797	47.8
Bi$_2$S$_3$ (Thioacetamide, 300 °C)	0.399	1.118	1.162	90.9	90.9	89.783	62.1
Bi$_2$S$_3$ (Thiourea, 300 °C)	0.399	1.118	1.162	90.9	90.9	89.772	93.7

Aiming to further evaluate the structural properties of the developed materials, Rietveld refinement was performed in order to determine the lattice parameters and crystallite sizes of the samples. The results are shown in Table 1.

It is reported that the crystallite size of photocatalysts may exert a profound influence on their performance in photocatalytic reactions. Smaller crystallite sizes typically correspond to larger SSAs and an increased number of surface defects, providing more active sites for adsorption and catalytic reactions [23]. This increased surface area enhances the accessibility of reactant molecules to catalytic sites, thereby improving the photocatalyst's efficiency in converting light energy into chemical energy. Additionally, smaller crystallite sizes facilitate more efficient charge carrier transport within the material, minimizing recombination losses and enhancing charge separation efficiency [23–25].

Within this context, the information gathered in Table 1 shows that the calcination process resulted in increased crystallite sizes for the materials synthesized using thiourea and thioacetamide, which may hinder the photocatalytic

activity of these materials due to the loss of active sites available for surface-bound processes. Additionally, the Bi$_2$S$_3$ synthesized using ammonium sulfide displayed the lowest crystallite size among the calcined samples, which may indicate a superior photocatalytic activity for this material.

Aiming to study the morphology of the bismuth sulfides synthesized, the scanning electron micrographs of the uncalcined materials are shown in Fig. 2. Furthermore, the SSA of each sample was measured and reported in Fig. 2F.

The micrographs obtained reveal a significant impact of the sulfide precursor on the morphology of the resulting Bi$_2$S$_3$ photocatalysts. The materials synthesized using Na$_2$S and (NH$_4$)$_2$S display nodular particle structures, while the Bi$_2$S$_3$ synthesized with K$_2$S manifests rod-like particles. The thioacetamide-based material is composed of large particles with a spherical tendency, which may lower the SSA available for adsorption and photocatalysis, whereas the thiourea-based material is composed of rigid spherical nanoparticle agglomerates. This morphology is probably unfavorable regarding the photocatalytic process, as the
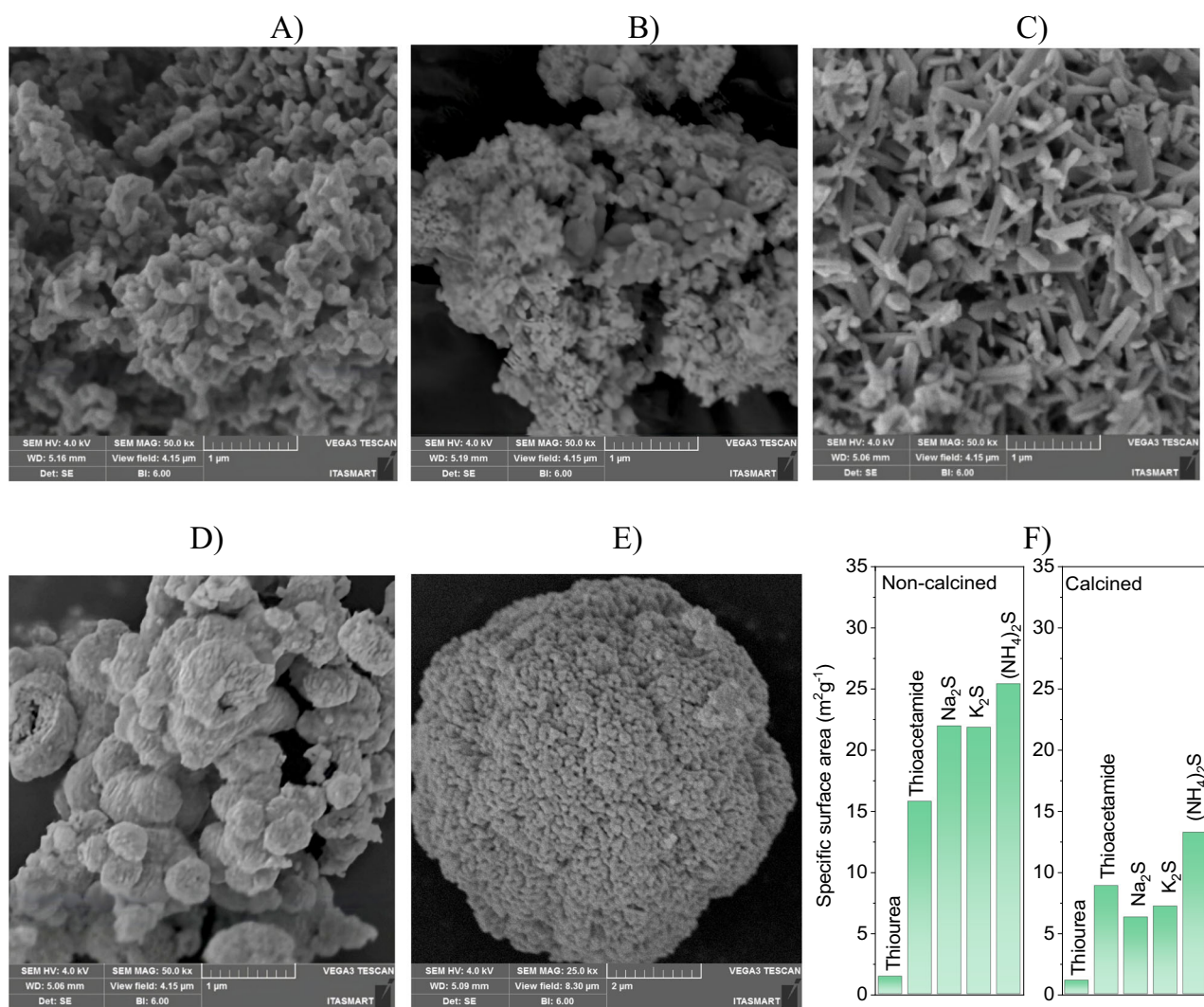
Fig. 2 Scanning electron micrographs (50000x) obtained for the materials synthesized using: **A** Na$_2$S; **B** (NH$_4$)$_2$S; **C** K$_2$S; **D** Thioacetamide; **E** Thiourea; **F** Specific surface area results

creation of dead zones inside the rigid clusters due to low light penetration is expected.

This variation in morphology suggests diverse nucleation and growth mechanisms influenced by the specific chemical properties and reaction conditions associated with each sulfide precursor. According to related literature, the nucleation process of sulfides is highly linked to the rate of S^{2-} released into the reactional system. When readily soluble sulfides (such as Na$_2$S, K$_2$S, and (NH$_4$)$_2$S) are used as sulfide sources, due to the high S^{2-} release rate, smaller particles are expected to be produced during the synthesis [26]. On the other hand, the lower reactivity of thiourea leads to a slower growth rate of the bismuth sulfide particles, resulting in the formation of larger hierarchical structures, as the large particles observed in Fig. 2E [27]. Thioacetamide, as an organic precursor with a higher S^{2-} ion release rate when compared to thiourea, reportedly leads

to the formation of particle aggregates with undefined shapes [27].

Interestingly, the presence of rod-shaped particles in the K$_2$S-derived Bi$_2$S$_3$ photocatalyst holds potential advantages for the photoactivation process. Rod-like structures typically possess a higher density of exposed edges and surface defects compared to spherical or nodular particles [28]. These edge defects serve as active sites for photocatalytic reactions, facilitating the separation and migration of photogenerated charge carriers. Consequently, the increased density of edge defects in rod-shaped particles may mitigate charge recombination processes during photonic excitation, leading to enhanced photocatalytic efficiency [29].

Regarding the SSAs obtained, the results are agreeable with the observed morphologies and XRD results. Prior to the calcination, the materials synthesized using K$_2$S, Na$_2$S, and (NH$_4$)$_2$S achieved the highest SSA values, which is
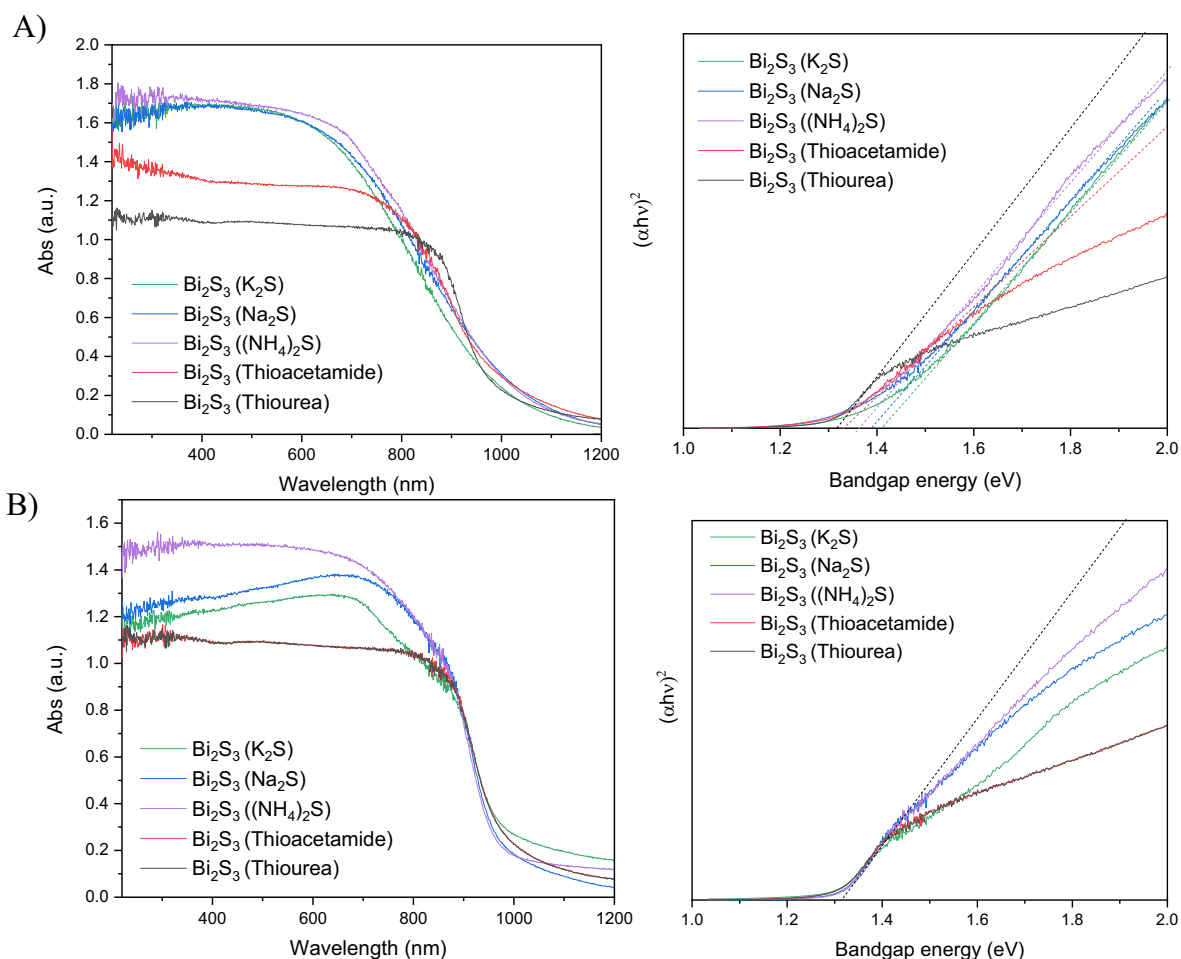
Fig. 3 Diffuse reflectance spectra and Kubelka-Munk plot for: **A** Uncalcined materials; **B** Calcined materials

probably derived from the amorphous nature of the samples, as their inherently disordered nature is commonly related to a high density of surface defects and high SSAs; on the other hand, the thiourea-based material had the smallest SSA, probably due to its unfavorable morphology.

Additionally, a noteworthy decrease in the SSA of all photocatalysts was observed post-calcination, a phenomenon that could potentially compromise both its adsorption capacity and photocatalytic efficiency. This result agrees with XRD data collected, as the calcination process can lead to sintering or agglomeration of particles, along with boosting crystallinity, resulting in a reduction of the SSA [30, 31]. This decrease in SSA diminishes the available active sites for adsorption, thereby limiting the material's ability to efficiently capture and hold target species for subsequent photocatalytic reactions. Therefore, it may be stated that the calcination process leads to antagonistic effects regarding the photocatalytic performance of the Bi_2S_3 samples, as a beneficial higher crystallinity towards change transfer is counterbalanced by the loss of SSA and higher crystallite sizes.

Finally, aiming to better understand the optical features of the Bi_2S_3 samples synthesized, Fig. 3 shows the diffuse reflectance spectra obtained for the materials. The bandgap energy (E_{gap}) of the materials was evaluated using the Kubelka-Munk function and Tauc plots [32].

As anticipated, diffuse reflectance analysis of the produced Bi_2S_3 samples reveals their exceptional ability to absorb radiation across a broad spectrum, extending up to 1000 nm. This remarkable characteristic renders them proficient in harnessing light energy not only within the visible spectrum but also within a significant portion of the near-infrared range. Upon closer examination, the bandgap energies of the calcined Bi_2S_3 materials exhibit a striking uniformity, typically measuring around 1.3 eV. In contrast, the non-calcined Bi_2S_3 variants demonstrate a slightly wider dispersion of bandgap energies, ranging from 1.3 to 1.4 eV; nonetheless, these measured bandgap energies align closely with those previously reported for Bi_2S_3 in pertinent scientific literature, affirming the validity of the proposed synthesis pathways and the materials' suitability for optoelectronic applications under sunlight [18].
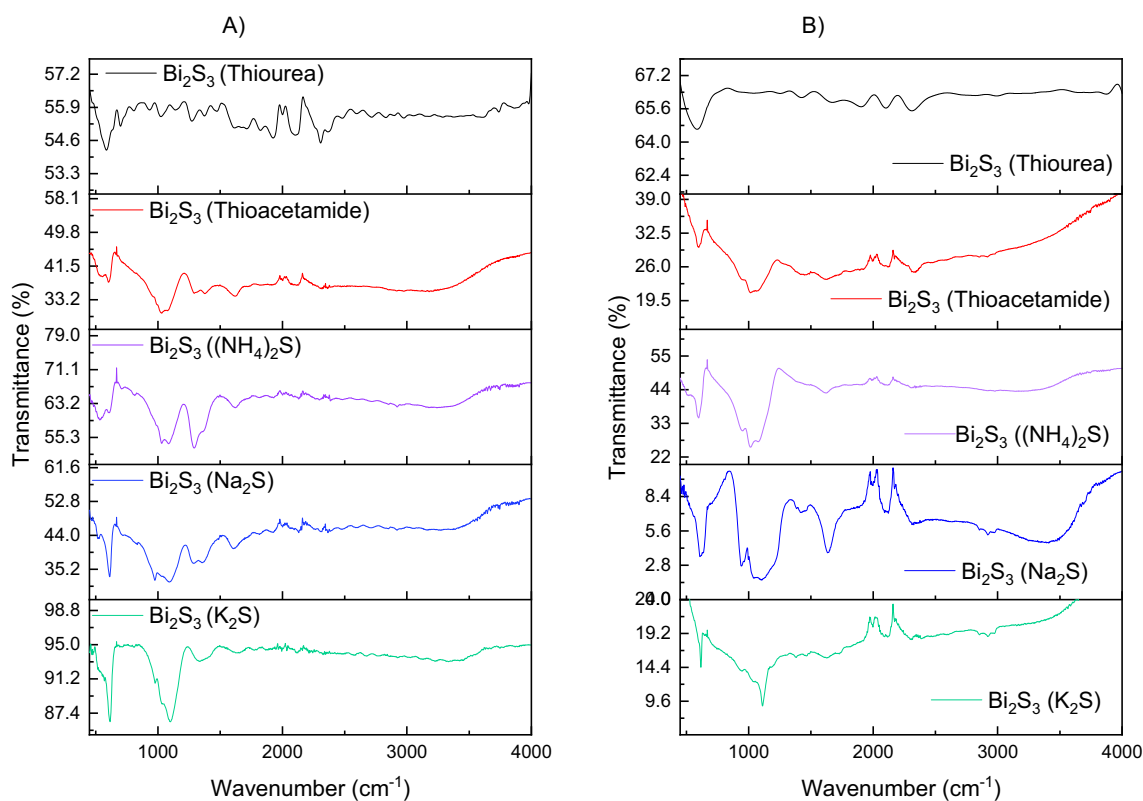
Fig. 4 Infrared spectra obtained for: **A** Uncalcined materials; **B** Calcined materials

Figure 4 shows the infrared spectra collected for the synthesized bismuth sulfides.

In the obtained spectra, the characteristic absorbance bands below 700 cm^{-1} are attributed to the Bi-S bonding, whereas the shoulder observed at 977 cm^{-1} is due to resonance interaction between vibrational modes of sulfur ions [33, 34]. The vibration bands around 1075 cm^{-1} can also be ascribed to Bi-S bonds. The band around 1620 cm^{-1} is related to the (O-H) bending vibrations of the adsorbed water, whereas the band at 3400 cm^{-1} is due to the presence of O-H vibration. Additionally, the bands around 1400 cm^{-1} can be linked to the presence of N-O groups, probably derived from the bismuth nitrate employed in the synthesis [35]. Notably, the presence of N-O groups was suppressed by the calcination of the samples, as the bands related to these groups nearly disappeared after the thermal treatment.

3.2 Photocatalytic reduction of Cr(VI)

The Bi$_2$S$_3$ samples were used for the photoreduction of Cr(VI) in aqueous media, under simulated sunlight. The results, along with the chronoamperometry performed for all Bi$_2$S$_3$ samples, are displayed in Fig. 5. Table 2 shows the results of the linear fit of the data to a pseudo-first-order kinetic model, where k_{app} stands for the apparent reaction rate constant [36].

Regarding the adsorption capacity of non-calcined materials, the Bi$_2$S$_3$ synthesized with (NH$_4$)$_2$S was the best adsorbent, with Na$_2$S and K$_2$S-based materials showing similar performances; this result agrees with the higher values of SSA observed for these materials, as the increased surface area facilitates the adsorption step of the photoreduction mechanism. The thioacetamide-based material achieved lower adsorption capacity, while the adsorption capacity of the thiourea-based material was negligible. Correlating the Cr(VI) photoreduction efficiency with the non-calcined photocatalysts morphologies and SSA, it can be noted that the Bi$_2$S$_3$ derived from K$_2$S, with a structure of small rods and high SSA, displayed the highest efficiency for Cr(VI) reduction, as anticipated due to the favorable properties of such morphology towards charge transfer during photonic activation. Photocatalysts consisting of nodular particles (synthesized using (NH$_4$)$_2$S and Na$_2$S), exhibited intermediate reduction potential, surpassing the material made with thioacetamide and its larger-sized spherical particles with intermediate SSA. Finally, the non-calcined thiourea-based material showed negligible activity for the Cr(VI) photoreduction, likely due to its inadequate morphology and low SSA. Additionally, the K$_2$S-based material achieved the highest current generation between non-calcined samples, which is probably related to its rod-like structure and lower charge recombination, corroborating its superior photocatalytic efficiency.
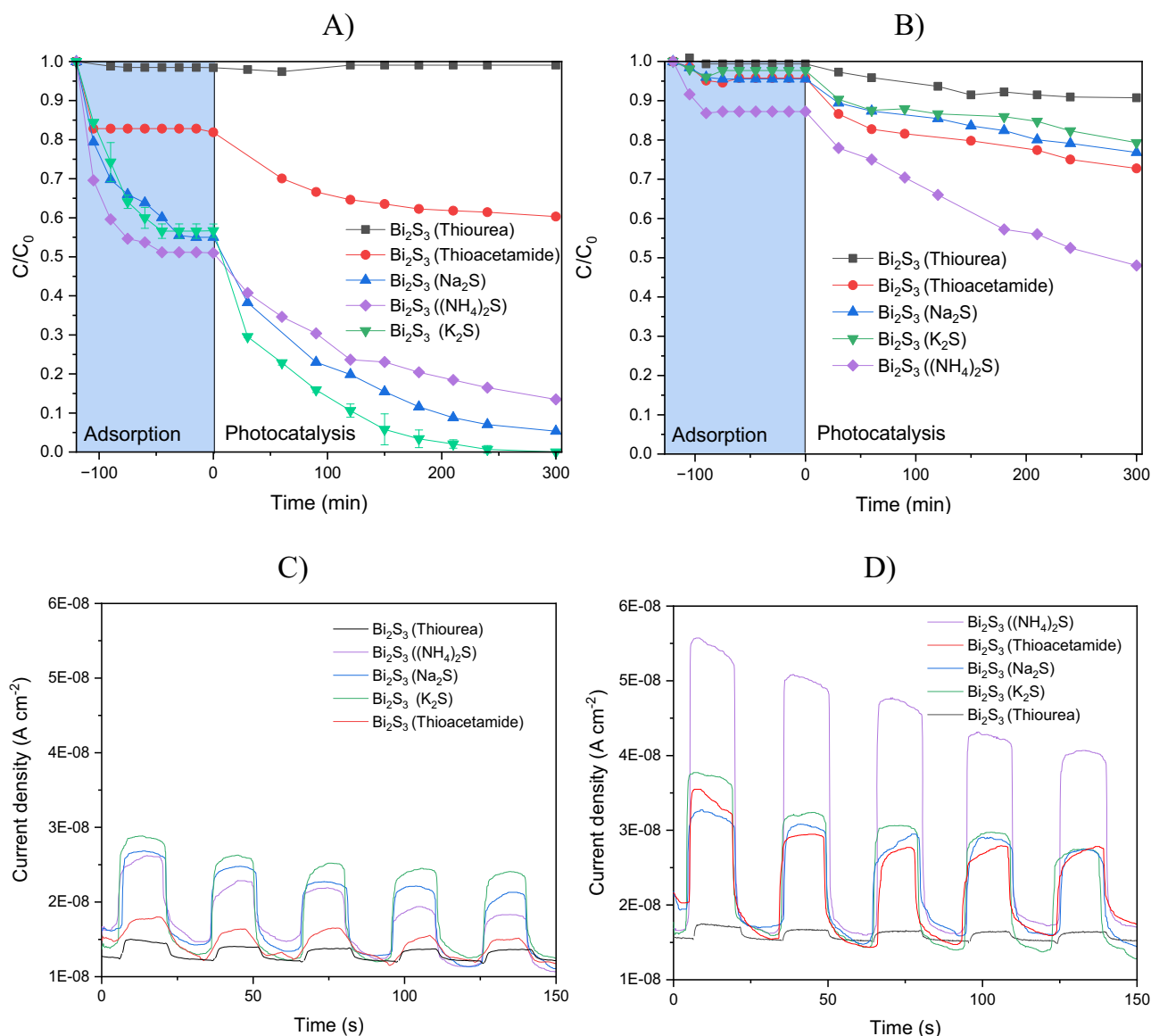
Fig. 5 Photoreduction of Cr(VI) using the developed bismuth sulfides: **A** Uncalcined; **B** Calcined; Chronoamperometry results for the Bi_2S_3 samples: **C** Uncalcined; **D** CalcinedTop of Form
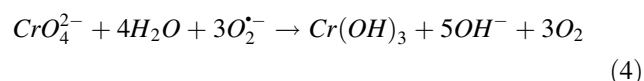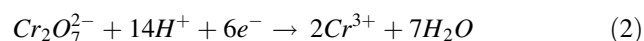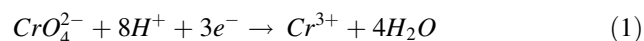
Calcined photocatalysts, in general, exhibited lower adsorption capacity compared to their non-calcined counterparts, which is probably linked to the loss of SSA after calcination. However, higher values of current density were observed in the chronoamperometry tests for all calcined materials (apart from the thiourea-based sample), indicating that the development of an organized crystalline structure is indeed favorable to the photoactivation process, due to more efficient charge transfer through the highly ordered atomic arrangement. Additionally, it can be seen that the (NH$_4$)$_2$S-based sample achieved the best adsorption capacity among the calcined materials, which can be also correlated to its higher SSA and lower crystallite size.

Considering that the non-calcined photocatalysts exhibited superior photoreduction efficiency compared to calcined samples, as observed through the k_{app} values in Table 2, it is evident that the adsorption process is of the utmost importance for the Cr(VI) photoreduction process to occur, even more than an increase in photocurrent generation. Typically, the photoreduction of the Cr(VI) involves the direct interaction of Cr^{6+}-based ions and the photogenerated electrons on the surface of the photocatalyst. Equations 1 and 2 exemplify the possible reduction reactions in the pH range used (pH = 5). Additionally, the reduction process may be carried out by the superoxide radical, which may be formed during the photocatalytic process due to the reduction of dissolved

Table 2 Kinetic parameters gathered from the photoreduction experiments

Material	Uncalcined		Calcined	
	k_{app} (min^{-1})	R^2	k_{app} (min^{-1})	R^2
Bi$_2$S$_3$ (K$_2$S)	0.0132	0.991	0.0005	0.962
Bi$_2$S$_3$ (Na$_2$S)	0.0083	0.992	0.0006	0.948
Bi$_2$S$_3$ ((NH$_4$)$_2$S)	0.0048	0.972	0.0020	0.988
Bi$_2$S$_3$ (Thioacetamide)	0.0013	0.961	0.0007	0.951
Bi$_2$S$_3$ (Thiourea)	–	–	0.0002	0.961

oxygen molecules (Eqs. 3 and 4) [37, 38].

$$CrO_4^{2-} + 8H^+ + 3e^- \rightarrow Cr^{3+} + 4H_2O \quad (1)$$

$$Cr_2O_7^{2-} + 14H^+ + 6e^- \rightarrow 2Cr^{3+} + 7H_2O \quad (2)$$

$$O_2 + e^- \rightarrow O_2^{\bullet-} \quad (3)$$

$$CrO_4^{2-} + 4H_2O + 3O_2^{\bullet-} \rightarrow Cr(OH)_3 + 5OH^- + 3O_2 \quad (4)$$

Considering that the E^0 of the Cr^{6+}/Cr^{3+} reduction reaction is close to 1.33 V (*vs.* NHE) and the conduction band (CB) potential of Bi$_2$S$_3$ is reported to be close to 0.12 V, it is evident that the CB of the bismuth sulfides produced is sufficient to promote the desired reduction reaction [39]. However, it must be noted that the E^0 involved in the superoxide formation is equal to −0.33 V, rendering the generation of said active radical unlikely during the photonic excitation of the Bi$_2$S$_3$ photocatalyst [40]. Therefore, to verify the effect of the photogenerated electrons and superoxide radicals during the photoreduction reaction, scavenging tests were performed using the uncalcined K$_2$S-based bismuth sulfide aiming to clearly define the impact of each active species during the process. The results are shown in Fig. 6.

Firstly, Fig. 6 demonstrates that the N$_2$ purging posed no major effect on the overall Cr(VI) photoreduction by the Bi$_2$S$_3$, making it clear that the presence of oxygen in the reactional system is unrelated to the overall efficiency of the reduction reaction; therefore, the notion that the superoxide plays no role in the proposed photocatalytic process is corroborated. Additionally, the test employing citric acid as a hole scavenger led to a major increase in the photoreduction efficiency, which can be explained by the suppression of the recombination process between photogenerated charges [41]. Finally, the test performed in the presence of silver nitrate as an electron scavenger led to a major reduction in the Cr(VI) photoreduction efficiency [42]. Thus, it is clear that the Cr(VI) photoreduction is mainly dependent on its direct interaction with photogenerated electrons on the
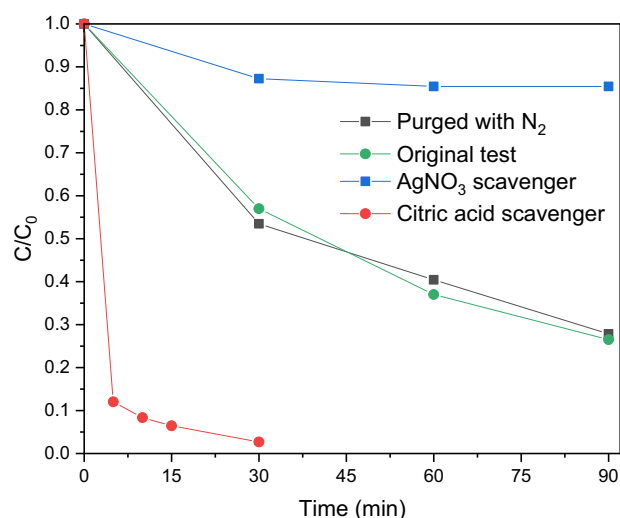

Fig. 6 Scavenging tests using the uncalcined K$_2$S-based bismuth sulfide

surface of the Bi$_2$S$_3$ (Eqs. 1 and 2). In this case, the adsorption step plays a major role in the mechanism involved in the reaction, as the chrome-based species must be adsorbed on the surface of the photocatalyst in order to capture the electrons donated by the photocatalyst; consequently, even materials with high photocurrent generation will not be able to promote the photoreduction reaction of the Cr(VI) if the adsorption capacity is hindered, as the low interaction between the species will halt the overall quantum efficiency of the process [39].

Hence, the major effect of the adsorption capacity on the overall efficiency of Cr(VI) reduction by the produced bismuth sulfides is elucidated, as materials with higher SSA and adsorption capacities yielded better results for Cr(VI) photoreduction. It also becomes evident that the thermal treatment of the bismuth sulfide samples imposes significant drawbacks on the material's performance due to the loss of adsorption capacity. Finally, while calcination may serve certain purposes such as enhancing crystallinity and photocurrent generation, its adverse impact on the performance of the bismuth sulfide samples underscores the necessity for nuanced optimization strategies in photocatalytic applications towards Cr(VI) reduction processes.

Figure 7 evaluates the influence of multiple operational processes, such as initial concentration, temperature, and pH, on the Cr(VI) photoreduction efficiency by the optimal bismuth sulfide photocatalyst (uncalcined Bi$_2$S$_3$-K$_2$S).

As Fig. 7A shows, the initial concentration of Cr(VI) significantly influences the photoreduction efficiency of the proposed photocatalytic process. A decline of the apparent reaction rate constant can be observed in the tests with higher concentrations, which can be ascribed to the limited
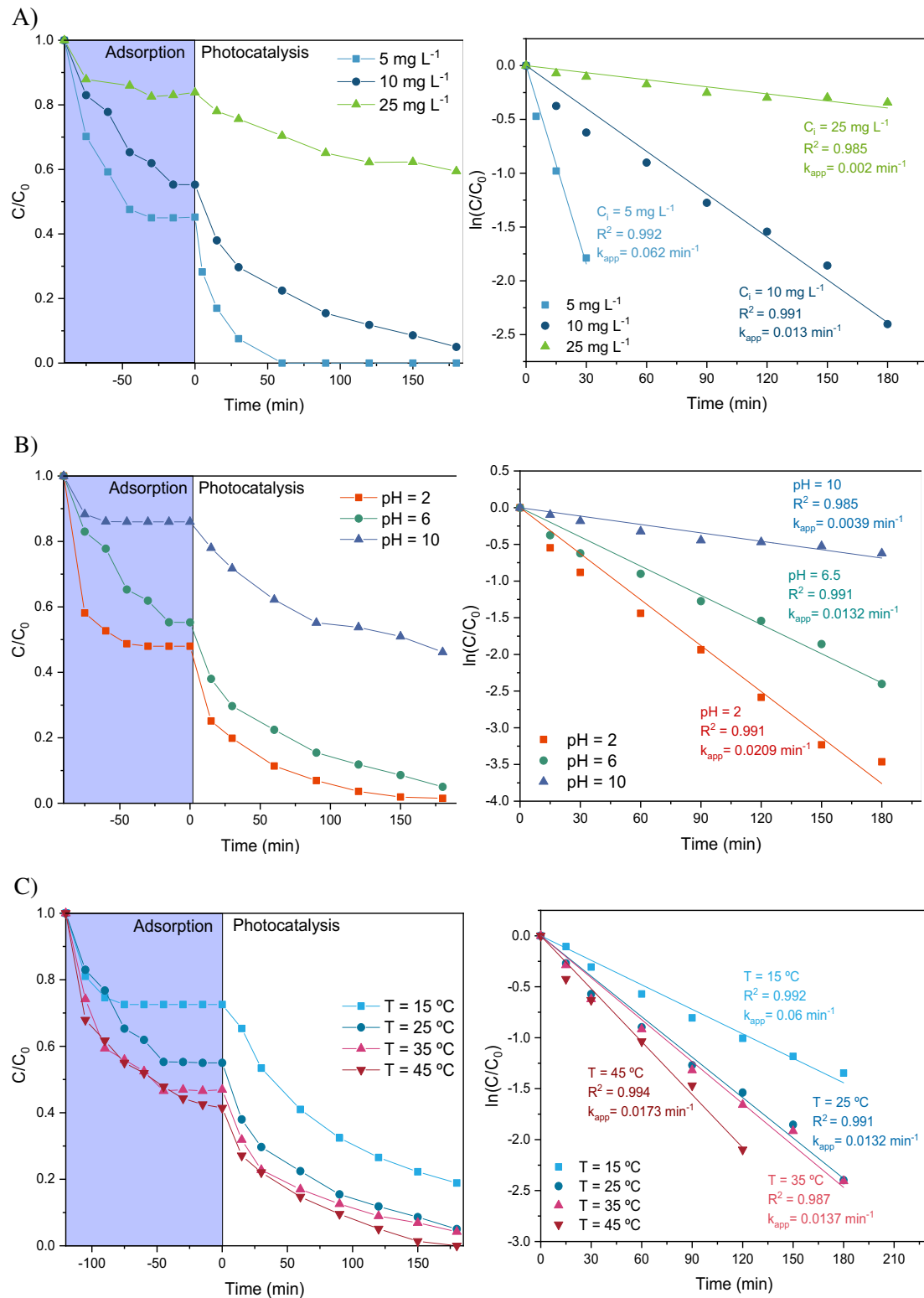
Fig. 7 **A** Effect of initial concentration on the Cr(VI) photoreduction; **B** Effect of pH on the Cr(VI) photoreduction; **C** Effect of temperature on the Cr(VI) photoreduction
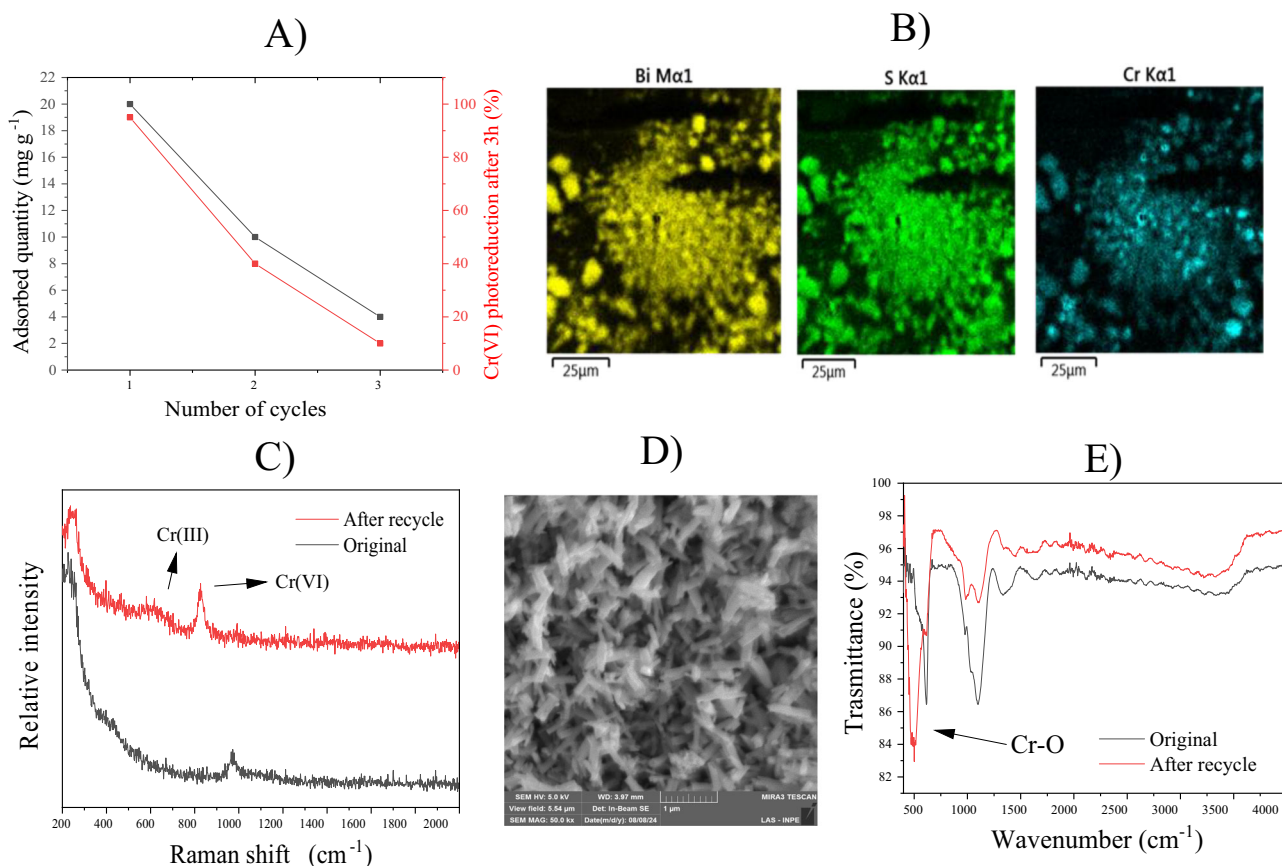
Fig. 8 A Results of Cr(VI) photoreduction after 3 cycles; **B** Elemental mapping of the recycled Bi_2S_3 sample; **C** Raman spectra of the original and recycled Bi_2S_3 sample; **D** Scanning electron micrograph of the recycled sample (50000x); **E** Infrared spectra of the original and recycled samples

availability of reactive species during the tests, as an excessive concentration of Cr(VI) is likely to saturate the surface available for the adsorption and photocatalytic steps to take place. Considering the above-demonstrated importance of photogenerated electrons for the reduction process, the negative effect of higher Cr(VI) concentrations in the proposed setup is likely related to the fact that such electrons will act as the limiting reactant, as under a fixed set of operating conditions the number of photogenerated electrons remains constant. Consequently, the ratio between Cr(VI) and photogenerated electrons is expected to control the kinetics of the photoreduction reaction; as this ratio increases, electrons become the limiting reactant, resulting in the reduction of the Cr(VI) photoreduction efficiency [43].

As for the pH effect (Fig. 7B), the results show that an increase in alkalinity is not beneficial to the photoreduction efficiency of the bismuth sulfide. Considering the point of zero charge determined for the bismuth sulfide employed in the tests ($pH_{pzc} = 6.2$), the material will be negatively charged as the pH is increased, hindering the adsorption of the CrO_4^{2-} and $Cr_2O_7^{2-}$ species. As described previously, the adsorption of the chromate ions is of paramount

importance to the photoreduction reaction; therefore, the decrease in adsorption led by the increase in pH can explain the drop in photocatalytic efficiency [43]. Additionally, Eqs. (1) and (2) evidence that the photoreduction reaction is dependent on the presence of H^+ ions, leading to the conclusion that lower pH values will be favorable towards the proposed process [43].

Finally, the modification of the temperature of the reactional system (Fig. 7C) also influenced the efficiency of the photoreduction reaction. The data obtained showed that higher temperatures are linked to higher adsorption capacities by the bismuth sulfide, indicating that the adsorption process is endothermic [44]. Thus, as lower temperatures led to reduced adsorption capacities, the photoreduction of Cr(VI) was hindered.

Figure 8 shows the results of photoreduction after recycling the bismuth sulfide produced using K_2S under multiple photoreduction cycles, as well as the characterization of the recycled sample.

The recycling results (Fig. 8A) show that the Bi_2S_3 sample is not able to maintain its efficiency between cycles of Cr(VI) photoreduction. Particularly, the Bi_2S_3 efficiency loss follows closely the drop in the adsorption capacity of

Table 3 Comparison between the results obtained in this work and related literature for Cr(VI) reduction

Material	Concentration	pH	% reduction	Reference
Bi_2S_3	$10\,mg\,L^{-1}$	6	95% (3 h)	This work
TiO_2-C dots	$10\,mg\,L^{-1}$	3	100% (2.5 h)	[47]
ZnO-C dots	$10\,mg\,L^{-1}$	6	100% (5 h)	[48]
ZrO_2	$10\,mg\,L^{-1}$	2	90% (5 h)	[49]
V_2O_5/g-C_3N_4	$20\,mg\,L^{-1}$	–	90% (1.5 h)	[50]
Bi_2S_3/MOF	$20\,mg\,L^{-1}$	5	100% (2 h)	[51]

the photocatalyst, further indicating that these factors are closely related. The efficiency reduction observed is likely caused by the saturation of the Bi_2S_3 surface by chrome-based components during each cycle. As the elemental mapping of the recycled sample (Fig. 8B) shows, its surface is homogeneously covered by the chrome element, even if no major difference can be noted in its morphology (Fig. 8D). The Raman spectrum of the recycled bismuth sulfide shows the appearance of two bands, located at ~550 and $830\,cm^{-1}$, which can be related to the presence of trivalent and hexavalent chrome species, respectively [45]. Additionally, the infrared spectrum of the recycled sample shows that a band related to Cr(III)-O antisymmetric stretching vibration emerged after 3 cycles of reuse, characteristic of hydrated chromium oxide [46]. Thus, it is indicated that the formation of Cr(III) precipitates over the reaction sites of the bismuth sulfide, along with the adsorbed Cr(VI) species, may have undermined the adsorptive and photocatalytic properties of the photocatalyst [47].

Finally, Table 3 shows a comparison between the results of Cr(VI) photoreduction obtained in this work and related literature under sunlight.

Table 3 shows that the Cr(VI) photoreduction results obtained in this work are well within the values reported in related literature, indicating that the optimized bismuth sulfide synthesized in this work is a promising material for practical applications.

4 Conclusion

It is concluded that the sulfide source plays a pivotal role in both the structural characteristics and photocatalytic performance of Bi_2S_3. The initial step of adsorption of Cr(VI) onto the photocatalysts acted as a linchpin for the subsequent photoreduction process, with a clear relation to the SSAs and morphologies observed for each sample. While calcination led to an enhancement of some of the materials' properties (crystallinity and photocurrent generation), it also resulted in the reduction of SSA and adsorption capacity, compromising the overall efficiency of the materials.

Remarkably, it is the uncalcined materials characterized by amorphous structures and heightened adsorption capacities that emerge as the frontrunners in Cr(VI) photoreduction efficiency. Among these, the K_2S-based material stands out as the best photocatalyst, achieving 100% Cr(VI) reduction after 5 h. This result is likely attributed to its high surface area and the favorable rod-shaped morphology of its particles, which may facilitate charge transfer during photonic activation. The scavenging tests indicate that the photoreduction of Cr(VI) is mainly related to its direct reaction with photogenerated electrons. Regarding the impact of operational parameters, it was defined that lower concentrations, lower pHs, and higher temperatures favor the reaction rate constant of the photoreduction reaction. The recycle tests show that the best bismuth sulfide produced (uncalcined using K_2S) is unable to maintain its efficiency after multiple cycles, probably due to the formation of chrome-based compounds on the surface of the photocatalyst, occluding its active sites.

Author contributions Nicolas Perciani de Moraes: Formal analysis; Investigation; Methodology; Software; Validation; Visualization; Roles/Writing—original draft; Writing—review & editing. Pedro Malavota Ribeiro: Formal analysis; Investigation; Methodology; Validation; Software; Visualization; Roles/Writing—original draft. Bruno Henrique Baena da Silva: Formal analysis; Investigation; Methodology; Validation; Software; Visualization; Roles/Writing—original draft. Tiago Moreira Bastos Campos—Formal analysis; Investigation; Methodology; Validation; Software; Visualization; Roles/Writing—reviewed draft. Gilma Patrocinio Thim—Formal analysis; Investigation; Methodology; Validation; Software; Visualization; Writing—reviewed draft. Marcos Roberto de Vasconcelos Lanza: Formal analysis; Funding acquisition; Investigation; Methodology; Project administration; Software; Supervision; Validation; Visualization; Roles/Writing—original draft; Writing—review & editing. Liana Alvares Rodrigues: Formal analysis; Funding acquisition; Investigation; Methodology; Project administration; Software; Supervision; Validation; Visualization; Roles/Writing—original draft; Writing—review & editing.

Compliance with ethical standards

References

1. Rahman Z, Thomas L, Chetri SPK, Bodhankar S, Kumar V, Naidu R (2023) A comprehensive review on chromium (Cr) contamination and Cr(VI)-resistant extremophiles in diverse extreme environments. Springer Berlin Heidelberg. https://doi.org/10.1007/s11356-023-26624-y

2. Pratush A, Kumar A, Hu Z (2018) Adverse effect of heavy metals (As, Pb, Hg, and Cr) on health and their bioremediation strategies: a review. Int Microbiol 21:97–106. https://doi.org/10.1007/s10123-018-0012-3

3. Bhati A, Anand SR, Saini D, Gunture, Sonkar SK (2019) Sunlight-induced photoreduction of Cr(VI) to Cr(III) in wastewater by nitrogen-phosphorus-doped carbon dots. Npj Clean Water 2:1–9. https://doi.org/10.1038/s41545-019-0036-z

4. Sharma P, Singh SP, Parakh SK, Tong YW (2022) Health hazards of hexavalent chromium (Cr (VI)) and its microbial reduction. Bioengineered 13:4923–4938. https://doi.org/10.1080/21655979.2022.2037273

5. Owlad M, Aroua MK, Daud WAW, Baroutian S (2009) Removal of hexavalent chromium-contaminated water and wastewater: a review. Water Air Soil Pollut 200:59–77. https://doi.org/10.1007/s11270-008-9893-7

6. Xia S, Song Z, Jeyakumar P, Shaheen SM, Rinklebe J, Ok YS, Bolan N, Wang H (2019) A critical review on bioremediation technologies for Cr(VI)-contaminated soils and wastewater. Crit Rev Environ Sci Technol 49:1027–1078. https://doi.org/10.1080/10643389.2018.1564526

7. Banu SK, Stanley JA, Sivakumar KK, Arosh JA, Taylor RJ, Burghardt RC (2017) Chromium VI—Induced developmental toxicity of placenta is mediated through spatiotemporal dys-regulation of cell survival and apoptotic proteins. Reprod Toxicol 68:171–190. https://doi.org/10.1016/j.reprotox.2016.07.006

8. Wang CC, Du XD, Li J, Guo XX, Wang P, Zhang J (2016) Photocatalytic Cr(VI) reduction in metal-organic frameworks: a mini-review. Appl Catal B Environ 193:198–216. https://doi.org/10.1016/j.apcatb.2016.04.030

9. Alharbi FF, Aman S, Ahmad N, Abdullah M, Abid AG, Manzoor S, Trukhanov S, Sayyed MI, Tishkevich D, Trukhanov A (2023) Investigation of photoreduction of Cr (VI) and electrocatalytic properties of hydrothermally produced novel CoFe2O4/ZnO nanostructure. Solid State Sci 143:107278. https://doi.org/10.1016/j.solidstatesciences.2023.107278

10. Islam JB, Furukawa M, Tateishi I, Katsumata H, Kaneco S (2019) Photocatalytic reduction of hexavalent chromium with nanosized TiO2 in presence of formic acid. ChemEngineering 3:1–10. https://doi.org/10.3390/chemengineering3020033

11. Barrera-Díaz CE, Lugo-Lugo V, Bilyeu B (2012) A review of chemical, electrochemical and biological methods for aqueous Cr(VI) reduction. J Hazard Mater 223–224:1–12. https://doi.org/10.1016/j.jhazmat.2012.04.054

12. Gaya UI (2014) Heterogeneous photocatalysis using inorganic semiconductor solids. Springe Sci 9789400777:1–213. https://doi.org/10.1007/978-94-007-7775-0

13. Wang M, Fang G, Liu P, Zhou D, Ma C, Zhang D, Zhan J (2016) Fe 3 O 4 @β-CD nanocomposite as heterogeneous Fenton-like catalyst for enhanced degradation of 4-chlorophenol (4-CP). Appl Catal B Environ 188:113–122. https://doi.org/10.1016/j.apcatb.2016.01.071

14. Zhang S, Ou X, Xiang Q, Carabineiro SAC, Fan J, Lv K (2022) Research progress in metal sulfides for photocatalysis: from activity to stability. Chemosphere 303. https://doi.org/10.1016/j.chemosphere.2022.135085

15. Helal A, Salem AMS, El-Hout SI (2024) Highly efficient visible light photoreduction of Cr(VI) via PANI/Bi2S3 Z-scheme behavior. J Photochem Photobiol A Chem 447:115232. https://doi.org/10.1016/j.jphotochem.2023.115232

16. Bernechea M, Cao Y, Konstantatos G (2015) Size and bandgap tunability in Bi2S3 colloidal nanocrystals and its effect in solution processed solar cells. J Mater Chem A 3:20642–20648. https://doi.org/10.1039/c5ta04441c

17. Ajiboye TO, Onwudiwe DC (2021) Bismuth sulfide based compounds: properties, synthesis and applications. Results Chem 3:100151. https://doi.org/10.1016/j.rechem.2021.100151

18. Li X, Jun L, Xiao J, Xu Y, Yang C, Tang J, Zhou K, Gong X, Zhou X, Zou H (2022) Study on the relationship between Bi2S3 with different morphologies and its photocatalytic hydrogen production performance. J Anal Sci Technol 13. https://doi.org/10.1186/s40543-022-00325-6

19. de Sousa Ribeiro LA, Thim GP, Alvarez-Mendez MO, dos Reis Coutinho A, de Moraes NP, Rodrigues LA (2018) Preparation, characterization, and application of low-cost açaí seed-based activated carbon for phenol adsorption. Int J Environ Res 12:755–764. https://doi.org/10.1007/s41742-018-0128-5

20. APHA (2017) Standard Methods for the Examination of Water and Wastewater. Federation. Water Environmental American Public Health Association (APHA), Washington, DC, USA

21. Perciani de Moraes N, da Silva Rocha R, Caetano Pinto da Silva ML, Bastos Campos TM, Thim GP, Landers R, Rodrigues LA (2020) Facile preparation of Bi-doped ZnO/β-Bi2O3/Carbon xerogel composites towards visible-light photocatalytic applications: effect of calcination temperature and bismuth content. Ceram Int 46:23895–23909. https://doi.org/10.1016/j.ceramint.2020.06.166

22. de Moraes NP, Silva FN, da Silva MLCP, Campos TMB, Thim GP, Rodrigues LA (2018) Methylene blue photodegradation employing hexagonal prism-shaped niobium oxide as heterogeneous catalyst: effect of catalyst dosage, dye concentration, and radiation source. Mater Chem Phys 214:95–106. https://doi.org/10.1016/j.matchemphys.2018.04.063

23. Wang X, Sø L, Su R, Wendt S, Hald P, Mamakhel A, Yang C, Huang Y, Iversen BB, Besenbacher F (2014) The influence of crystallite size and crystallinity of anatase nanoparticles on the photo-degradation of phenol. J Catal 310:100–108. https://doi.org/10.1016/j.jcat.2013.04.022

24. Kim DS, Han SJ, Kwak SY (2007) Synthesis and photocatalytic activity of mesoporous TiO2 with the surface area, crystallite size, and pore size. J Colloid Interface Sci 316:85–91. https://doi.org/10.1016/j.jcis.2007.07.037

25. Hurum DC, Agrios AG, Gray KA, Rajh T, Thurnauer MC (2003) Explaining the enhanced photocatalytic activity of Degussa P25 mixed-phase TiO2 using EPR. J Phys Chem B 107:4545–4549. https://doi.org/10.1021/jp0273934

26. Sabet M, Salavati-Niasari M, Esmaeili E (2016) Synthesis of zinc sulfide nanostructures with different sulfur sources via mild hydrothermal route: investigation of crystal phase and morphology. J Inorg Organomet Polym Mater 26:738–743. https://doi.org/10.1007/s10904-016-0374-y

27. Chen J, Qin S, Song G, Xiang T, Xin F, Yin X (2013) Shape-controlled solvothermal synthesis of Bi2S3 for photocatalytic reduction of CO2 to methyl formate in methanol. Dalt Trans 42:15133–15138. https://doi.org/10.1039/c3dt51887f

28. Vallejos S, Pizúrová N, Gràcia I, Sotelo-Vazquez C, Čechal J, Blackman C, Parkin I, Cané C (2016) ZnO rods with exposed {100} facets grown via a self-catalyzed vapor-solid mechanism and their photocatalytic and gas sensing properties. ACS Appl Mater Interfaces 8:33335–33342. https://doi.org/10.1021/acsami.6b12992

29. de Moraes NP, Bacani R, da Silva MLCP, Campos TMB, Thim GP, Rodrigues LA (2018) Effect of Nb/C ratio in the morphological, structural, optical and photocatalytic properties of novel and inexpensive Nb2O5/carbon xerogel composites. Ceram Int 44:6645–6652. https://doi.org/10.1016/j.ceramint.2018.01.073

30. Mediouni N, Guillard C, Dappozze F, Khrouz L, Parola S, Colbeau-Justin C, Amara ABH, Ben Rhaiem H, Jaffrezic-Renault N, Namour P (2022) Impact of structural defects on the

photocatalytic properties of ZnO. J Hazard Mater Adv 6:100081. https://doi.org/10.1016/j.hazadv.2022.100081

31. Golsheikh AM, Kamali KZ, Huang NM, Zak AK (2018) Effect of calcination temperature on performance of ZnO nanoparticles for dye-sensitized solar cells. Powder Technol 329:282–287. https://doi.org/10.1016/j.powtec.2017.11.065

32. Jubu PR, Chahrour KM, Muhammad A, Lamido S, Kan-Hausa U, Landi S, Obaseki OS, Gundu AA, Chahul HF, Yam FK (2023) Considerations about the determination of optical bandgap from diffuse reflectance spectroscopy using the Tauc plot. 1–19. https://doi.org/10.21203/rs.3.rs-2654236/v1

33. Fenelon E, Ni'Am AC, Wang YF, You SJ (2022) Study of the potential of La/Bi2S3 catalyst for photodegradation of acid yellow 42 dye under visible light. J Nanomater 2022. https://doi.org/10.1155/2022/2990466

34. Singh A, Chauhan P, Verma A, Yadav BC (2024) Interfacial engineering enables polyaniline-decorated bismuth sulfide nanorods towards ultrafast metal–semiconductor-metal UV-Vis broad spectra photodetector. Adv Compos Hybrid Mater 7:1–17. https://doi.org/10.1007/s42114-024-00878-7

35. Astuti Y, Fauziyah A, Nurhayati S, Wulansari AD, Andianingrum R, Hakim AR, Bhaduri G (2016) Synthesis of α-Bismuth oxide using solution combustion method and its photocatalytic properties. IOP Conf Ser Mater Sci Eng 107. https://doi.org/10.1088/1757-899X/107/1/012006

36. de Moraes NP, Torezin FA, Jucá Dantas GV, de Sousa JGM, Valim RB, da Silva Rocha R, Landers R, da Silva MLCP, Rodrigues LA (2020) TiO2/Nb2O5/carbon xerogel ternary photocatalyst for efficient degradation of 4-chlorophenol under solar light irradiation. Ceram Int 46:14505–14515. https://doi.org/10.1016/j.ceramint.2020.02.249

37. Xu J, Dai Y, Shi Y, Zhao S, Tian H, Zhu K, Jia H (2020) Mechanism of Cr(VI) reduction by humin: role of environmentally persistent free radicals and reactive oxygen species. Sci Total Environ 725:138413. https://doi.org/10.1016/j.scitotenv.2020.138413

38. Asoubar S, Mehrizad A, Behnajady MA, Ramazani ME, Gharbani P (2023) Hexavalent chromium reduction and Rhodamine B degradation by visible-light-driven photocatalyst of stannum indium sulfide-samarium vanadate. Npj Clean Water 6. https://doi.org/10.1038/s41545-023-00246-w

39. Yuan G, Li F, Li K, Liu J, Li J, Zhang S, Jia Q, Zhang H (2021) Research progress on photocatalytic reduction of Cr(VI) in polluted water. Bull Chem Soc Jpn 94:1142–1155. https://doi.org/10.1246/bcsj.20200317

40. Li J, Jiang M, Zhou H, Jin P, Cheung KMC, Chu PK, Yeung KWK (2019) Vanadium dioxide nanocoating induces tumor cell death through mitochondrial electron transport chain interruption. Glob Challenges 3. https://doi.org/10.1002/gch2.201800058

41. Yi XH, Wang FX, Du XD, Wang P, Wang CC (2019) Facile fabrication of BUC-21/g-C3N4 composites and their enhanced photocatalytic Cr(VI) reduction performances under simulated sunlight. Appl Organomet Chem 33:1–11. https://doi.org/10.1002/aoc.4621

42. Shen X, Zheng T, Yang J, Shi Z, Xue Q, Liu W, Shan S, Wong MH (2020) Removal of Cr(VI) from acid wastewater by BC/ZnFe2O4 magnetic nanocomposite via the synergy of absorption-photocatalysis. ChemCatChem 12:4121–4131. https://doi.org/10.1002/cctc.202000619

43. Valari M, Antoniadis A, Mantzavinos D, Poulios I (2015) Photocatalytic reduction of Cr(VI) over titania suspensions. Catal Today 252:190–194. https://doi.org/10.1016/j.cattod.2014.10.014

44. Adebayo GB, Adegoke HI, Fauzeeyat S (2020) Adsorption of Cr(VI) ions onto goethite, activated carbon and their composite: kinetic and thermodynamic studies. Appl Water Sci 10:1–18. https://doi.org/10.1007/s13201-020-01295-z

45. Vaskova H (2016) Raman microscopic detection of chromium compounds. MATEC Web Conf 76:4–7. https://doi.org/10.1051/matecconf/20167605012

46. Li H, Zhang H, Luo M, Dong Y, Xu H, Cheng X, Cai Z (2021) Adsorption of vanadium with amorphous hydrated chromium oxide. Water Pract Technol 16:1410–1420. https://doi.org/10.2166/wpt.2021.078

47. Li Y, Liu Z, Wu Y, Chen J, Zhao J, Jin F, Na P (2018) Carbon dots-TiO2 nanosheets composites for photoreduction of Cr(VI) under sunlight illumination: favorable role of carbon dots. Appl Catal B Environ 224:508–517. https://doi.org/10.1016/j.apcatb.2017.10.023

48. Khare P, Bhati A, Anand SR, Gunture, Sonkar SK (2018) Brightly fluorescent zinc-doped red-emitting carbon dots for the sunlight-induced photoreduction of Cr(VI) to Cr(III). ACS Omega 3:5187–5194. https://doi.org/10.1021/acsomega.8b00047

49. Bashirom N, Kian TW, Kawamura G, Matsuda A, Razak KA, Lockman Z (2018) Sunlight activated anodic freestanding ZrO2 nanotube arrays for Cr(VI) photoreduction. Nanotechnology 29:375701. https://doi.org/10.1088/1361-6528/AACCBD

50. Dadigala R, Bandi R, Gangapuram BR, Dasari A, Belay HH, Guttena V (2019) Fabrication of novel 1D/2D V2O5/g-C3N4 composites as Z-scheme photocatalysts for CR degradation and Cr (VI) reduction under sunlight irradiation. J Environ Chem Eng 7:102822. https://doi.org/10.1016/j.jece.2018.102822

51. Wang Y, Kang C, Xiao K, Wang X (2020) Fabrication of Bi2S3/MOFs composites without noble metals for enhanced photoreduction of Cr (VI). Sep Purif Technol 241:116703. https://doi.org/10.1016/j.seppur.2020.116703